Rydberg electromagnetically induced transparency in a large Hilbert space

Yongmei Xue,[1] Liping Hao,[1] Yuechun Jiao,[1,2] Xiaoxuan Han,[1] Suying Bai,[1] Jianming Zhao,[1,2,*] and Georg Raithel[1,3]

[1]*State Key Laboratory of Quantum Optics and Quantum Optics Devices, Institute of Laser Spectroscopy, Shanxi University, Taiyuan 030006, People's Republic of China*

[2]*Collaborative Innovation Center of Extreme Optics, Shanxi University, Taiyuan 030006, China*

[3]*Department of Physics, University of Michigan, Ann Arbor, Michigan 48109-1120, USA*

(Received 25 September 2018; revised manuscript received 28 March 2019; published 30 May 2019)

We study Rydberg electromagnetically induced transparency (EIT) of cesium atoms in a magnetic field. The ladder level scheme consists of ground ($6S_{1/2}$), excited ($6P_{3/2}$), and Rydberg ($48D_{5/2}$) levels. The relevant 96 relevant magnetic sublevels are coupled to each other via coherent coupling and decay. A quantum Monte Carlo wave-function (QMCWF) approach is employed to solve the quantum master equation. The simulated EIT probe-absorption spectra and their magnetic-field dependence are compared with results of a cold-atom experiment, in which we perform an *in situ*, atom-based measurement of a rapidly decaying eddy-current magnetic field. The EIT spectrum in the magnetic field has two dominant lines with a Zeeman splitting of 5.6 MHz per gauss, which are employed to measure the magnetic field. The QMCWF results show good agreement with the experiment, exhibit additional spectroscopic features, and provide insights into the optical-pumping dynamics, radiation-pressure effects, and the relation of these phenomena with the EIT behavior.

DOI: 10.1103/PhysRevA.99.053426

I. INTRODUCTION

Rydberg atoms, atoms with principal quantum numbers $n \gtrsim 10$, have been widely investigated in recent years due to their exaggerated characteristics compared to those of ground-state atoms [1], such as large size and dipole moment (scaling as n^2), and strong long-range van der Waals interactions (scaling as n^{11}). These properties make Rydberg atoms perfect candidates for quantum information processing [2], studies of optical nonlinearities in new regimes [3,4], and nonequilibrium phenomena [5–7]. Due to their tenuous atomic binding and their dense quantum-mechanical level structure, Rydberg atoms are very sensitive to external fields. They have, for instance, large dc electric polarizabilities that scale as n^7, as well as strong resonant electric-dipole couplings with microwave and THz fields that scale as n^2. These features make Rydberg atoms attractive for field measurement purposes [8–13]. In much of this work, electromagnetically induced transparency (EIT), a quantum interference effect [14], has been used as an optical, nondestructive probe for Rydberg-atom behavior and response [15]. Rydberg EIT, a ladder-type variant of EIT, is suitable to probe Rydberg states in both room-temperature vapor cells [11] as well as in cold-atom clouds [16]. Rydberg EIT serves as a readout in measurements of weak [8] and strong [17] microwave electric fields in vapor cells, and it is relevant in Rydberg-atom-based quantum information processing [18]. EIT has also been used to investigate Cs Rydberg atoms in magnetic fields up to ∼0.01 T [19] and Rb Rydberg and $5D_{5/2}$ atoms in fields up to ∼0.6 T [20,21].

In EIT on level schemes with magnetic sublevels, multiple sublevels are, typically, coupled either directly by the optical EIT fields, or by spontaneous decay, or both. For atomic species with large nuclear spin, this leads to large Hilbert spaces of coupled states. For instance, in [11] there were 52 and in [19] 64 relevant levels. In such systems, EIT and optical pumping can mutually depend on each other [19]. The complexity of the problem can further increase due to explicit dependencies of the EIT laser fields on position and time, as well as atomic motion during the atom-field interaction time. For instance, in cold-atom systems one may have to account for radiation-pressure-induced atom acceleration and velocity diffusion. In the present paper, we consider a Rydberg-EIT system in cesium that consists of the $6S_{1/2}$ ground, $6P_{3/2}$ intermediate, and $nD_{5/2}$ Rydberg states. We model EIT and optical pumping in this 96-level system, as well as radiation-pressure effects applicable to cold-atom implementations. The model is based on quantum Monte Carlo wave-function simulations (QMCWF [22,23]).

The work extends our previous study of *S*-type Rydberg atoms in a vapor cell experiment [19] to laser-cooled *D*-type Rydberg atoms, which have more magnetic substates. The expanded model also includes the atomic center-of-mass motion as a dynamic variable that allows us to account for the effect of radiation pressure and photon-recoil-induced velocity diffusion, which is important in cold-atom EIT due to the low initial velocity of the laser-cooled atoms, and because the atom-field interaction is sufficiently long for the velocity and angular-momentum distribution of the atoms to change during the EIT probe. We apply the QMCWF results to calibrate *in situ* magnetic-field measurements within a cloud of laser-cooled cesium atoms, which serve as a magnetic-field probe. In our experimental testing platform, the magnetic field consists of a homogeneous field provided by a pair of Helmholtz coils, B_0, and a decaying eddy-current-induced magnetic field, $B_e(t)$. The QMCWF

*Corresponding author: zhaojm@sxu.edu.cn

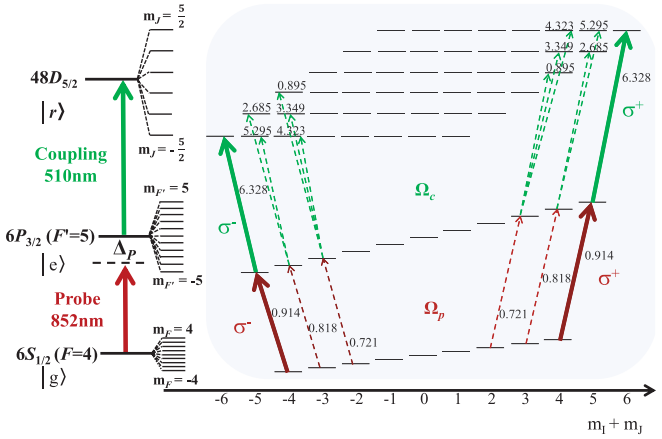

FIG. 1. Typical energy-level scheme. The 510 nm coupling laser drives the $|6P_{3/2}F' = 5\rangle \rightarrow |48D_{5/2}\rangle$ Rydberg transitions. The 852 nm probe laser is used to measure absorption on the $|6S_{1/2}, F = 4\rangle \rightarrow |6P_{3/2}, F' = 5\rangle$ transition. In the depicted case, a magnetic field pointing along z splits the magnetic sublevels, and both coupling and probe lasers are linearly polarized along x (transverse to the magnetic field). The arrows indicate the strongest transitions driven by the lasers. The numbers show Rabi frequencies (in MHz) for typical beam intensities used in our experiments.

model we develop also allows for straightforward simulation of time-dependent protocols, such as probe-laser frequency scans.

II. RYDBERG-EIT SCHEME IN WEAK MAGNETIC FIELDS

Before introduction of the QMCWF model, we illustrate the EIT system of interest and provide a qualitative discussion of the expected behavior. The level scheme, shown in Fig. 1, consists of the cesium ground state, $|g\rangle = |6S_{1/2}, F = 4\rangle$, the intermediate excited state, $|e\rangle = |6P_{3/2}, F' = 5\rangle$, and the Rydberg state, $|r\rangle = |nD_{5/2}\rangle$. The scheme constitutes a cascade EIT system with numerous magnetic sublevels and Zeeman line splittings. In the examples provided here, the principal quantum number $n = 48$; the results are, however, applicable over a range of n. The probe laser beam (wavelength 852 nm) drives the lower transition ($|g\rangle \rightarrow |e\rangle$), while a strong 510 nm laser beam couples the intermediate to the Rydberg state ($|e\rangle \rightarrow |r\rangle$).

The ground and intermediate levels, $|g\rangle$ and $|e\rangle$, are in the linear Zeeman regime, with magnetic quantum numbers $m_{F,g}$ and $m_{F,e}$ and respective hyperfine g factors $g_{F,g} = 0.25$ and $g_{F,e} = 0.4$. The $48D_{5/2}$ Rydberg level is in the Zeeman regime of the fine structure and in the Paschen-Back regime of the hyperfine structure. The Lande g_J factor of the $48D_{5/2}$ level is $g_{J,r} = 1.2$. The $48D_{5/2}$ hyperfine structure is neglected due to its vanishing size. (An estimate provided in [24] yields an upper limit for the hyperfine coupling parameter A_{hfs}, $48D_{5/2}$ on the order of 1 kHz.) In both the Zeeman and Paschen-Back regimes, all levels have well-defined $m_I + m_J$ (the horizontal axis in Fig. 1). The $6S$ and $6P$ levels have, in addition, well-defined hyperfine quantum numbers, F and $m_F = m_I + m_J$. The level shifts from the field-free positions, visualized in Fig. 1, are

$$\Delta_g = \mu_B B g_{F,g} m_{F,g}, \quad \Delta_e = \mu_B B g_{F,e} m_{F,e},$$
$$\Delta_r = \mu_B B (g_{J,r} m_J + g_I m_I), \tag{1}$$

where μ_B is the Bohr magneton and g_I is the g factor of the cesium nucleus, $g_I = -0.000\,398\,853\,95$ [25]. The separation between adjacent Rydberg m_J levels is $B \times 1.68$ MHz/G. The nuclear Zeeman shifts of the Rydberg level are only several kHz and are neglected, i.e., for our purposes the Rydberg levels are m_I degenerate.

In a cold-atom system with weak magnetic fields and conditions as in Fig. 1, optical pumping by the x-polarized probe field optically pumps the ground-state atoms towards the outer m sublevels. Ignoring Doppler shifts, which are sub-MHz in typical cold-atom systems, the magnetic subcomponents of the probe absorption line shift by amounts $\mu_B B[(m_{F,g}(g_{F,e} - g_{F,g})) \pm g_{F,e}]$, which, for the outermost transitions, amounts to $\pm(1.40$ MHz/G$) \times B$. Therefore, ignoring any EIT effects, the probe resonance line is expected to widen, as a whole, at a rate of about 2.8 MHz/G. In Fig. 1, the dominant EIT lines are attributed to the outermost transitions indicated by the thickest arrows. In a Doppler-shift-free system, EIT requires two-photon resonance between the ground and Rydberg levels, while the intermediate level can be off-resonant by amounts up to several linewidths of the probe transition. In a weak magnetic field, the EIT line splits and the EIT components shift from the center of the probe absorption line. Since the magnetic field shifts the outermost Rydberg levels by $\pm(4.2$ MHz/G$) \times B$ and the ground levels by $\pm(1.4$ MHz/G$) \times B$, for the case of fixed coupling-laser frequency the EIT lines in the probe absorption spectrum shift outward by amounts given by the difference of these shifts, namely by ± 2.8 MHz/G $\times B$. Hence, in the case of Fig. 1, the dominant Zeeman-split EIT line pair is expected to separate at a rate of 5.6 MHz/G, which is twice as much as the probe-line broadening. Therefore, with increasing B field the EIT lines become increasingly off resonant from the center of the probe absorption line. In fields larger than about 3 to 4 G the dominant EIT lines will become invisible because they move out of the probe absorption line.

While this qualitative explanation suffices to understand some trends in experimental results, an accurate description is needed to account for all transitions, not just the outermost cascades in Fig. 1. Also, the full EIT model should include Doppler shifts and their modifications due to radiation pressure, as well as optical pumping and its time dependence. Further, the model should be able to accommodate the spatial and temporal structure of atom-field interactions due to laser beam diameters and profiles, atom velocities, laser scans, etc. Finally, in the model we develop we account for all intermediate hyperfine levels, $F' = 2$ to 5, and atom decay into the lower ground-state hyperfine level is taken into account, with the possibility of (incoherent) repumping. Hence the model is applicable to magnetic fields up to a few hundred G, in which the ground- and intermediate-state Zeeman shifts become nonlinear and enter the Paschen-Back regime.

III. SIMULATION OF RYDBERG EIT IN HIGHLY DIMENSIONAL HILBERT SPACES

In the geometry given in Fig. 1, all $6S_{1/2}$, $6P_{3/2}$, and $48D_J$ states are coupled to each other by the optical fields and the spontaneous decay of the excited states. For cesium, the nuclear spin $I = 7/2$, leading to a total of 128 levels. If the fine-structure splitting of the $48D_J$ levels is much larger than the Rydberg-level Zeeman shifts, the $J = 3/2$ levels may be omitted, reducing the state space to 96. This state count is sufficiently large to seek the benefits of the quantum Monte Carlo wave-function (QMCWF) method [22,23] to determine the density matrix, rather than to directly solve the quantum master equation (which has about 5000 coupled equations). Since the numerical effort to obtain a "quantum trajectory" with the QMCWF method scales as the square of the Hilbert-space dimension, while that of the quantum master equation scales as its fourth power, the QMCWF can be more readily scaled up to higher dimensions than the master equation. The larger the dimension, the more advantageous the QMCWF method becomes. The QMCWF method has, for instance, previously been applied to model laser cooling [26,27] and wave-packet dynamics [28,29] in near-resonant optical lattices with quantized center-of-mass motion, with basis sizes of up to ∼1000. In the present work, we employ the method to model Rydberg-EIT systems with large internal-state Hilbert spaces. We also take advantage of the fact that the QMCWF allows for straightforward integration of the atomic center-of-mass motion as a classical variable.

Some fundamentals of the QMCWF model applied to highly dimensional Rydberg-EIT systems are discussed in our previous work [19], in which we have studied the Zeeman effect of Ryderg-EIT spectra in vapor cells using S-type Rydberg atoms. In the following, we provide some additional details about the method. The QMCWF relies upon the calculation of a large number N of "quantum trajectories," whose evolution consists of segments of deterministic Hamiltonian propagation (with a non-Hermitian effective Hamiltonian that includes atomic decay) and discrete, stochastic quantum jumps. At time $t = 0$, the beginning of the atom-field interaction, the state of the system is initialized in a randomly selected magnetic sublevel of the $6S_{1/2}$ ground state, and the center-of-mass velocity is randomly chosen from a Maxwell distribution given by the temperature of the atomic gas. During the segments of deterministic Hamiltonian evolution, the state is driven by the EIT fields and the wave-function norm decays in proportion with the probabilities and the decay rates associated with the excited-state components of the wave function (here, the $6P_{3/2}$ hyperfine magnetic sublevels). Quantum jumps occur when the wave-function norm drops below a random number s, which is drawn at the beginning of each new leg of Hamiltonian evolution. The quantum jumps simulate the detection of a spontaneously emitted photon of any of the three possible polarization states, σ^+, σ^-, or π, with emission directions that follow the respective electric-dipole radiation patterns. The jumps are instantaneous, i.e., they don't require any simulated time. The jumps are effected by "jump operators" that project the excited-state part of the wave function onto ground-state wave functions in accordance with the randomly selected type of emission, σ^+, σ^-, or π. The probabilities for the three types of decay, σ^+, σ^-, or π, are computed from basic rules of quantum measurement. In each individual jump, a random number is drawn to select the type of decay and another one is drawn to pick a photon emission angle from the electric-dipole radiation pattern for the selected type of decay. The wave function is re-initialized according to the von Neumann wave-function reduction postulate, and the atomic center-of-mass velocity is updated to account for the absorption of a probe photon and the emission of an outgoing photon at the selected emission angle. In the jump, excited-state Zeeman coherence is (partially) transferred into ground-state Zeeman coherence. The wave-function norm is reset to 1 and a new random number s is drawn for the next jump. After the jump, Hamiltonian evolution resumes and proceeds until the norm drops below the value of s and the next jump occurs. The simulated evolution therefore alternates between Hamiltonian dynamics and quantum jumps, with use of random numbers to effect the jumps. The simulation proceeds until the desired atom-field interaction time is reached. One realization of the procedure yields one quantum trajectory. Typically, 1000 to 10 000 quantum trajectories are sufficient for an approximate solution of the density operator. From a number of N "quantum trajectories," the density operator of the atomic ensemble is computed via

$$\hat{\rho}(t) = \frac{1}{N}\sum_{i=1}^{N} \frac{|\psi_i(t)\rangle\langle\psi_i(t)|}{\langle\psi_i(t)|\psi_i(t)\rangle}. \tag{2}$$

It is noted that the QMCWF simulation includes the changes in atomic velocity that result from the recoils of the absorbed probe-laser photons and the spontaneously emitted photons (which depend on the selected emission angles). The atomic velocities, $v_i(t)$, are propagated as classical variables in each quantum trajectory $i = 1 \ldots N$. The resultant time-dependent probe- and coupling-laser Doppler shifts, $\mathbf{k}_P \cdot \mathbf{v}_i(t)$ and $\mathbf{k}_C \cdot \mathbf{v}_i(t)$, vary in time and are included in the Hamiltonian dynamics of $|\psi_i(t)\rangle$ between the quantum jumps. Therefore, the QMCWF is suitable to simulate radiation-pressure effects, and it is applicable to both cold-atom and vapor-cell implementations.

The QMCWF returns many observables of interest, including the probe absorption coefficient, the probe photon scattering rate, the probe refractive index, the expectation value and the variance of the atom distribution over the magnetic substates $m_{F,g}$, and the atomic center-of-mass velocity distribution. For instance, the absorption coefficient for the probe field, $\alpha_P(t)$, and the EIT spectral line profiles are calculated from

$$\alpha_P(t) = \frac{4\pi n_V}{\lambda_P \epsilon_0 E_0}\mathrm{Im}\left(\sum_{m_{F,e},m_{F,g}} [\epsilon_P \cdot \mathbf{d}_{m_{F,e},m_{F,g}}]\,\rho_{m_{F,g},m_{F,e}}(t)\right), \tag{3}$$

with probe polarization vector ϵ_P, ground level $|6S_{1/2}, F = 4, m_{F,g}\rangle$, intermediate level $|6P_{3/2}, F = 5, m_{F,e}\rangle$, atom volume density n_V, probe wavelength λ_P, probe electric-field amplitude E_0, and electric-dipole operator matrix elements $\mathbf{d}_{m_{F,e},m_{F,g}} = \langle F' = 5, m_{5,e}|\hat{\mathbf{d}}|F = 4, m_{4,g}\rangle$. Due to selection rules, the double sum reduces to a single sum. For instance,

for π-polarized probe it is $m_{F,g} = m_{F,e} =: m_F$, and

$$\alpha_{P,\pi}(t) = \frac{4\pi n_V}{\lambda_P \epsilon_0 E_0} \mathrm{Im}\left(\sum_{m_F} d_{z,m_{F,e},m_{F,g}} \rho_{m_{F,g},m_{F,e}}(t) \right). \quad (4)$$

The refractive index of the medium is

$$n(t) = 1 + \frac{n_V}{\epsilon_0 E_0} \mathrm{Re}\left(\sum_{m_{F,e},m_{F,g}} [\epsilon_P \cdot \mathbf{d}_{m_{F,e},m_{F,g}}] \rho_{m_{F,g},m_{F,e}}(t) \right). \quad (5)$$

The probe absorption coefficient $\alpha_P(t)$ can also be obtained directly, in a transparent fashion, by acquisition of the simulated photon scattering rate per atom per time. This is achieved by recording the average rate at which the quantum jumps occur. In our simulations, we determine α_P from both Eq. (3) and from direct photon counting, and we check the results for agreement. It is noted that the photon counting results carry shot noise due to the finite number N of atoms used in the QMCWF, in close analogy with the photon shot noise that could be observed in an experiment. Here, we typically find a number of $N = 10^4$ quantum trajectories to be sufficient to achieve a satisfactory level of simulated shot noise in the data.

IV. EXPERIMENTAL APPLICATION

A. Testing setup

QMCWF simulations are employed to analyze data from a cold-atom magnetic-field measurement experiment. We use a standard cesium magneto-optical trap (MOT) with a temperature $\sim$100 μK and peak density $\sim 10^{10}$ cm^{-3}, shown in Fig. 2(a). The probe laser beam (wavelength 852 nm) drives

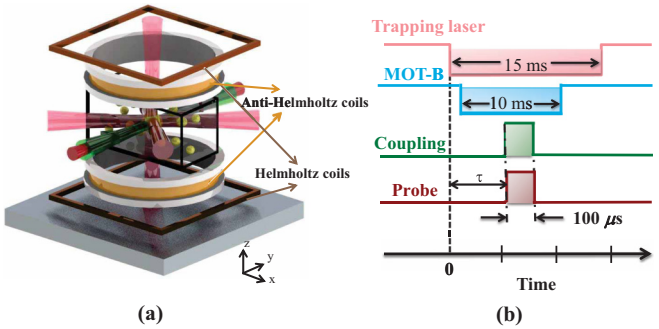

(a) (b)

FIG. 2. (a) Sketch of the experimental setup. Six beams of a 852 nm laser and the anti-Helmholtz coils constitute a cesium magneto-optical trap. 510 nm coupling and 852 nm probe laser beams are counterpropagated through the MOT cloud, probing the three-level Rydberg-EIT system. The probe beam is passed through a dichroic mirror (not shown), and the transmitted probe light is detected with a single-photon counting module (SPCM). When the MOT magnetic field is switched off, a transient eddy-current magnetic field is generated by currents induced in an aluminum plate located below the experimental chamber. A separate pair of Helmholtz coils is employed to superimpose an additional magnetic field over the eddy-current magnetic field. (b) Timing diagram. After turning off the MOT-coil current and the trapping beams, the Helmholtz coils are turned on at time τ. To probe the magnetic field, Rydberg-EIT coupling and probe lasers are turned on for 100 μs and scanned across the resonance.

the lower transition ($|g\rangle \rightarrow |e\rangle$), while a strong 510 nm laser beam couples the intermediate to the Rydberg state ($|e\rangle \rightarrow |r\rangle$). The resultant Rydberg-EIT spectrum is used for nondestructive detection of the Rydberg levels [15] and their Zeeman splittings. which lend themselves to an efficient, *in situ*, fast magnetic-field measurement tool. In our experimental implementation, the probe beam is produced by a diode laser (DLpro, Toptica) and is locked to the ground-state transition, $|g\rangle \rightarrow |e\rangle$, using polarization spectroscopy [30]. The probe laser is counterpropagated with the coupling-laser beam through the cold-atomic cloud. The coupling beam is provided by a commercial laser (Toptica TA-SHG110) with linewidth $\sim$1 MHz. Further details of the experiment have been described previously [31,32].

In each experimental cycle, at time $\tau = 0$ we turn off the MOT-coil current and the trapping beams. The eddy currents generated in an aluminum plate beneath the chamber [see Fig. 2(a)] produce a decaying eddy-current magnetic field, $B_e(t)$, at the atom cloud location. After a time τ, we switch on the current in a pair of Helmholtz coils, adding a magnetic field B_0 to the eddy-current field. The field $B_0 = I_0 \times 1.81$ G/A was changed by varying the current I_0 of the Helmholtz coils [see Fig. 2(a)], with a calculated calibration factor 1.81 G/A. Both fields point along the z direction. To measure the field $B(t) = B_e(t) + B_0$, Rydberg-EIT probe and coupling lasers are turned on at time τ for 100 μs, as shown in Fig. 2(b). Using a double-pass acousto-optic modulator (AOM), the probe laser frequency is swept across the $|6S_{1/2}, F = 4\rangle \rightarrow |6P_{3/2}, F' = 5\rangle$ transition from +15 MHz to −15 MHz relative to the field-free transition. During the scan, the Rydberg-EIT spectra are recorded using a data acquisition card (NI-PCI-6542) and processed with a Labview program. The magnetic-field sampling rate is given by the scan duration, which is 100 μs in the present case. The decay of the eddy-current field $B_e(t)$ is probed by stepping the delay time τ between subsequent realizations of the experiment.

The coupling laser has a fixed frequency resonant with the field-free $|6P_{3/2}, F' = 5\rangle$ to $|48D_{5/2}\rangle$ transition. The repumping laser is kept on during the Rydberg-EIT measurement. Both probe and coupling lasers are linearly polarized in x direction, i.e., they consist of equal parts of σ^+ and σ^- components with respect to the z-quantization axis (which is parallel to B). Due to the dominance of the Rabi frequencies for transitions between the outermost magnetic substates and partial optical pumping, this configuration yields a pair of Rydberg-EIT lines that correspond to the σ^+-σ^+ and σ^--σ^- transitions indicated by the thick arrows in Fig. 1. Due to the Zeeman effect, this line pair is split by a frequency value γ_{Zee} that is proportional to $B(t)$. According to the discussion in Sec. II, the splitting should follow $\gamma_{Zee} = B(t) \times 5.6$ MHz/G.

B. Experimental and simulation results

In the first experiment, we use a fixed delay time of $\tau = 6$ ms after switching off the MOT. We vary the Helmholtz coils current I_0 and measure the resultant Rydberg EIT spectra. The radial Rabi frequency of the probe transition at the beam center is $\Omega_{p,r} \approx 2\pi \times 2.2$ MHz, corresponding to Rabi frequencies between the magnetic states ranging between $2\pi \times 0.1$ and $2\pi \times 1$ MHz, for x-polarized light (see Fig. 1).

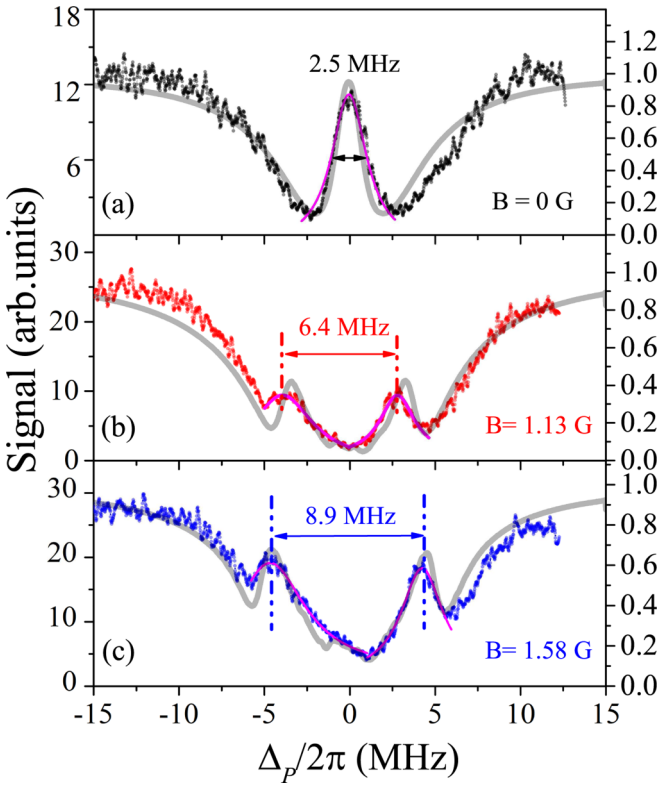

FIG. 3. Measurements of the Rydberg ($48D_{5/2}$) EIT spectra for the indicated magnetic fields. Lorentzian fits of the EIT peaks are employed to measure EIT linewidths and line separations. As seen in (a), the fitted FWHM width of the EIT line at zero field is $\gamma_{\rm EIT}/2\pi = 2.5$ MHz. The magnetic fields in (b) and (c) cause the EIT lines to Zeeman split into line pairs, resulting in the indicated peak-to-peak distances, γ_{Zee}. The gray solid lines show results of the quantum Monte Carlo wave-function model.

The exact value of $\Omega_{p,r}$ is not important; it only matters that $\Omega_{p,r} < \Gamma_e = 2\pi \times 5.2$ MHz and that the probe-pulse sweep is relatively short, to avoid the effects of line broadening and radiation pressure on the Rydberg-EIT spectra. The radial Rabi frequency of the coupling laser at the beam center is $\Omega_{c,r} \approx 2\pi \times 12$ MHz, corresponding to Rabi frequencies between magnetic states ranging from $2\pi \times 0.2$ to $2\pi \times 6$ MHz (see Fig. 1). The Rabi frequencies are estimated based on beam powers and diameters and have been validated by comparing experimental data with QMCWF simulations.

In Fig. 3, we present Rydberg EIT spectra obtained with currents $I_0 = -0.4$ A, 0.2 A, and 0.5 A, corresponding to net magnetic fields $B = B_0 + B_e$ ($\tau = 6$ ms) of $B = 0$ G, 1.13 G, and 1.58 G, respectively. The lower spectra show pairs of EIT peaks with a Zeeman splitting γ_{Zee}, while in the upper spectrum the Helmholtz current I_0 was adjusted to yield one EIT line of minimal width, equivalent to vanishing net magnetic field. Notably, $B = 0$ occurs at a nonzero current $I_0 = -0.4$ A. This means that at a delay time of $\tau = 6$ ms the eddy-current-induced field has a value of $B_e = 1.81$ G/A $\times$ 0.4 A $=$ 0.72 G, and a Helmholtz current of -0.4 A compensates the field generated by the eddy currents in the aluminum plate. The width of the EIT peak for $B = 0$, defined as the full width at half maximum (FWHM) of the peak, is $\gamma_{\rm EIT}/2\pi =$ 2.5 MHz [see Fig. 3(a)], as determined by a Lorentzian fit to the peak.

We vary the Helmholtz-coil current I_0 to change the net magnetic field at the atom cloud location. Two examples of Rydberg-EIT spectra with Zeeman splitting are displayed in Figs. 3(b) and 3(c). The peak-to-peak distances of the Zeeman-split EIT line pairs, γ_{Zee}, measured by Lorentzian fits to the EIT peaks spectra, are indicated in the figure. The results of the QMCWF simulations, shown as gray lines in Fig. 3, reproduce the EIT spectra and the Zeeman splittings very well. The agreement validates our assumption in Sec. II that the "outermost" three-level EIT systems indicated by the thick arrows in Fig. 1 dominate the EIT splitting behavior. The simulations also directly show that the splitting between the dominant EIT lines indeed follows $\gamma_{Zee} = B \times 5.6$ MHz/G.

The QMCWF results also reproduce the experimentally observed asymmetry of the spectra. It is found that the asymmetry is mostly due to the dynamic nature of the optical pumping that occurs in the course of the probe-frequency scan. As the $m_{F,g}$ distribution changes during the course of the 100-μs-long probe laser scan, the contributions of the different absorption channels change during the probe scan, leading to the asymmetry in the spectrum. Under the experimental conditions used, the spectra obtained for reversed probe-laser scan direction are near-perfect mirror images of the ones shown in Fig. 3. This proves that under the conditions in Fig. 3 the asymmetry of the spectra is only due to optical pumping and that Doppler shifts due to radiation pressure have a negligible effect. If radiation pressure had a substantial effect, the spectra for different signs of the probe-frequency chirp would not merely be mirror images of each other, because during a positive probe-laser chirp the radiation-pressure-induced acceleration tends to keep the atoms in resonance, while a negative chirp tends to tune the atoms faster out of resonance. Analyzing the center-of-mass velocity distributions returned by the QMCWF simulation, it is indeed seen that, for the case of Fig. 3, the velocity change due to radiation pressure during the entire scan only is about 0.1 m/s, corresponding to Doppler shifts on the order of 100 kHz. This is too small to become observable.

The QMCWF reveals additional details that are observable. For instance, in addition to the EIT line pairs that split at a rate of 5.6 MHz/G, the simulations and some of the experimental data such as in Figs. 3(b) and 3(c) exhibit a minor EIT feature near zero detuning. The QMCWF results show that the feature becomes tilted and washed out because of the scanning of the probe laser. Further, in the simulations it is seen that probe scans with longer scan durations yield more pronounced optical pumping, stronger asymmetries, as well as a clear effect of the sign of the laser chirp. As an example, in Fig. 4 we compare QMCWF transmission spectra and optical-pumping curves for scan durations of 100 μs and 1 ms. The respective radiation-pressure-induced velocities after completion of the scans are 0.1 m/s and 0.8 m/s.

To demonstrate that the QMCWF model applies over a range of magnetic fields and to illustrate the utility of Ryberg-EIT spectroscopy as an optical magnetic-field diagnostic, we have varied the Helmholtz-coil current I_0 in finer steps and recorded spectra equivalent to those in Fig. 3. In Fig. 5, we present the measured EIT Zeeman splittings, γ_{Zee} (black

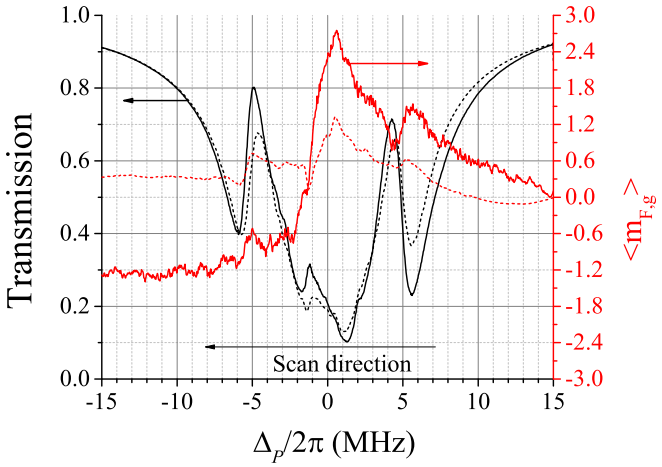

FIG. 4. Effect of scan duration in QMCWF results, for conditions that are otherwise identical with Fig. 3(c). The plot shows transmission spectra (left axis) and average $\langle m_{F,g} \rangle$ (right axis) as a function of probe frequency for scan durations of 100 μs (dashed) and 1 ms (solid). The magnitude of $\langle m_{F,g} \rangle$ reveals the degree and the dynamics of optical pumping.

filled circles) as a function of the magnetic field B. The solid line shows a linear fit through the data. The fit has a slope of 5.65 MHz/G, in close agreement with the value of 5.6 MHz/G found in the QMCWF results. The minor deviation is attributed to uncertainties in the Lorentzian fits to the Zeeman subcomponents in the EIT spectra (magenta lines in Fig. 3), and due to the calibration uncertainty of the Helmholtz-coil magnetic field.

C. Rydberg EIT with a time-dependent magnetic field

Rydberg EIT, and QMCWF as a tool to model Rydberg EIT in large Hilbert spaces, are both amenable to situations that require temporal resolution. As an example, we map the

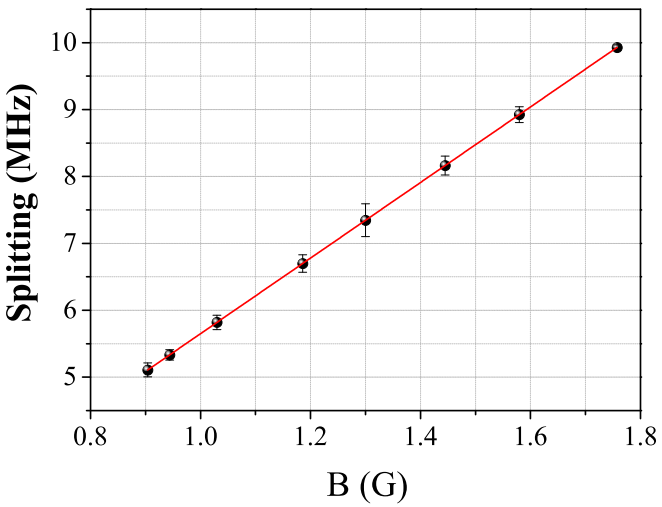

FIG. 5. Measurements (black filled circles) of Zeeman splitting, γ_{Zee}, as a function of magnetic field B. The data are averages over three measurements. The red solid line is a linear fit to the data, showing that $\gamma_{Zee} = B \times 5.65$ MHz/G.

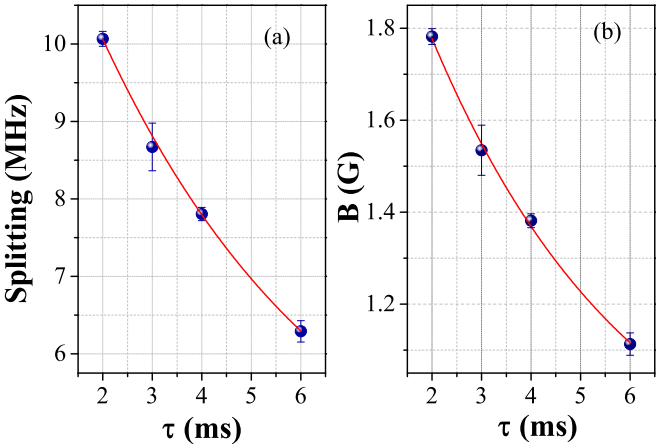

FIG. 6. Measurements of Zeeman splitting, γ_{Zee}, (a) and corresponding extracted magnetic field (b) as a function of delay time τ. The splitting and the eddy-current magnetic field closely follow the indicated exponential fits, which have a characteristic decay time of $\tau_0 = 4.85 \pm 0.77$ ms.

effects of eddy currents that are induced in the aluminum structure in Fig. 2(a) by switching off the MOT magnetic field. The eddy currents exponentially decrease as a function of delay time τ. In the following demonstration, we employ Rydberg EIT as explained in Sec. IV to measure the field and the eddy-current decay time. Dynamic Rydberg-EIT-based diagnostic translates to other situations with time-dependent fields.

We set the Helmholtz current I_0 at a value that compensates fixed environmental magnetic fields (Earth magnetic field, ion-pump fields, etc.) at late times, where the eddy currents have decayed. We then vary the delay time τ, see Fig. 2(b), to perform a series of measurements such as in Fig. 3. The measured Zeeman splittings, γ_{Zee}, and the corresponding eddy-current-induced magnetic-field values, B_e, are presented as a function of τ in Fig. 6. The measurements closely follow exponential fit functions with a $1/e$ decay time of $\tau_0 = 4.85 \pm 0.77$ ms. The measurement series reveals an eddy-current decay time of 4.85 ms in the aluminum plate, which is in line with miscellaneous data on aluminum that can be found online. An exact modeling of the particular value is not of interest in the present paper.

We finally comment on the overall utility of our test setup for magnetic-field diagnostics. The error bars in Fig. 5 indicate a root-mean-square uncertainty of the line splitting on the order of 130 kHz, corresponding to a magnetic-field uncertainty of 23 mG. Given the 100 μs probe time, the statistical magnetic-field uncertainty is 2.3×10^{-8} T/$\sqrt{\text{Hz}}$. We expect that this sensitivity could be improved by one to two orders of magnitude by using low-power, narrow-linewidth coupling and probe lasers. While a projected statistical field uncertainty of $\sim 2 \times 10^{-10}$ T/$\sqrt{\text{Hz}}$ is higher than other atomic magnetometers [33–39], the method may have specialized applications due to its high bandwidth, *in situ* measurement capability, calibration-free magnetic-field readout (shared with other atomic magnetometers), and potential simplicity (when implemented in vapor cells). One application relies in magnetic-field measurement and zeroing in

cold-atom clouds in vacuum systems that are inaccessible to physical field probes, and where methods such as Faraday rotation measurement or microwave spectroscopy cannot be applied.

V. CONCLUSION AND DISCUSSION

In summary, we have developed a QMCWF approach to model Rydberg-EIT systems with large Hilbert spaces. The QMCWF allows us to integrate the highly dimensional quantum master equation of the system. To test the method, we compare the QMCWF results with experimental Rydberg-EIT Zeeman spectra of Rydberg atoms in a cesium MOT. A controllable magnetic field, provided by a pair of Helmholtz coils, is superimposed over a decaying eddy-current field, which originates from eddy currents induced in an aluminum plate when switching off the MOT magnetic field. The Zeeman splitting, the optical-pumping behavior, and the effects of probe-light-induced radiation pressure are simulated and analyzed in detail using the QMCWF. Experimental and simulated results agree well. In the case studied, a pair of dominant Zeeman-split EIT lines are found to exhibit a splitting $\gamma_{Zee} = 5.65$ MHz/G. The Rydberg-EIT spectra are acquired in rapid sequence, with a scan time of 100 μs. This has allowed us to use the Rydberg-EIT field measurement method to diagnose the eddy-current decay time in our system. The method complements other position-resolved atomic [34–36] and diamond magnetometers [38] with several advantages, such as calibration-free, *in situ*, rapid magnetic-field measurement.

The work shows that the QMCWF is an efficient tool for modeling Rydberg EIT in large Hilbert spaces, as encountered in Rb and Cs Rydberg EIT. The QMCWF allows for the modeling of experiments and applications in great detail and for a wide variety of conditions. It is applicable to both cold-atom and vapor-cell studies and it allows for straightforward integration of time dependencies in laser field strengths, center-of-mass dynamics and the resultant time-dependent Doppler shifts, experimental shot noise, absorptive and dispersive effects, and so on. In the case at hand, we have used Rydberg EIT to diagnose dynamic, eddy-current-induced magnetic fields, a common issue in cold-atom experiments with switching coil systems. The method is based on atomic spectroscopy, is free of systematic shifts of the zero point and systematic calibration errors, and allows for *in situ* field measurement at the location of the cold atoms. The method may find applications for other *in situ* measurements of rapid magnetic-field transients. Since the Zeeman EIT spectra depend on light polarizations and exhibit time-dependent optical pumping, it should be possible to characterize magnitude and direction of varying magnetic fields in cold-atom systems. The sampling time of the magnetic field, currently at 100 μs, and the sampling rate can be greatly improved by implementing faster laser scans and photodiodes; the fundamental limit here is given by the intrinsic EIT response time (which is in the range of hundreds of nanoseconds). In the future, the QMCWF model may be scaled up to include a larger number of internal atomic levels in more complex atom-field interaction schemes, and to quantize the center-of-mass motion. In experimental studies, one may be able to directly observe radiation-pressure and optical-pumping effects present in cold-atom implementations, using time-delayed shadow imaging and Stern-Gerlach-type analysis of the populations in the magnetic sublevels.

ACKNOWLEDGMENTS

The work was supported by the National Key R&D Program of China (Grant No. 2017YFA0304203), the National Natural Science Foundation of China (Grants No. 61475090, No. 61675123, No. 61775124, and No. 11804202), Changjiang Scholars and Innovative Research Team University of Ministry of Education of China (Grant No. IRT 17R70), and the State Key Program of National Natural Science of China (Grants No. 11434007 and No. 61835007). G.R. acknowledges support by 111 project (Grant No. D18001) and the NSF (Grant No. PHY-1806809).

[1] T. F. Gallagher, *Rydberg Atoms* (Cambridge University Press, Cambridge, UK, 1994).
[2] D. Jaksch, J. I. Cirac, P. Zoller, S. L. Rolston, R. Côté, and M. D. Lukin, Phys. Rev. Lett. **85**, 2208 (2000).
[3] Y. O. Dudin and A. Kuzmich, Science **336**, 887 (2012).
[4] T. Peyronel, O. Firstenberg, Q.-Y. Liang, S. Hoffberth, A. V. Gorshkov, T. Pohl, M. D. Lukin, and V. Vuletić, Nature (London) **488**, 57 (2012).
[5] C. Carr, R. Ritter, C. G. Wade, C. S. Adams, and K. J. Weatherill, Phys. Rev. Lett. **111**, 113901 (2013).
[6] M. Marcuzzi, E. Levi, S. Diehl, J. P. Garrahan, and I. Lesanovsky, Phys. Rev. Lett. **113**, 210401 (2014).
[7] Z. Fu, L. Huang, Z. Meng, P. Wang, L. Zhang, S. Zhang, H. Zhai, P. Zhang, and J. Zhang, Nat. Phys. **10**, 110 (2014).
[8] J. A. Sedlacek, A. Schwettmann, H. Kübler, R. Löw, T. Pfau, and J. P. Shaffer, Nat. Phys. **8**, 819 (2012).
[9] C. L. Holloway, J. A. Gordon, S. Jefferts, A. Schwarzkopf, D. A. Anderson, S. A. Miller, N. Thaicharoen, and G. Raithel, IEEE Trans. Antennas Propag. **62**, 6169 (2014).
[10] H. Fan, S. Kumar, J. Sedlacek, H. Kübler, S. Karimkashi, and J. P. Shaffer, J. Phys. B: At. Mol. Phys. **48**, 202001 (2015).
[11] J. A. Sedlacek, A. Schwettmann, H. Kübler, and J. P. Shaffer, Phys. Rev. Lett. **111**, 063001 (2013).
[12] J. A. Gordon, C. L. Holloway, A. Schwarzkopf, D. A. Anderson, S. Miller, N. Thaicharoen, and G. Raithel, Appl. Phys. Lett. **105**, 024104 (2014).
[13] D. Barredo, H. Kübler, R. Daschner, R. Löw, and T. Pfau, Phys. Rev. Lett. **110**, 123002 (2013).
[14] K.-J. Boller, A. Imamoğlu, and S. E. Harris, Phys. Rev. Lett. **66**, 2593 (1991).
[15] A. K. Mohapatra, T. R. Jackson, and C. S. Adams, Phys. Rev. Lett. **98**, 113003 (2007).
[16] K. J. Weatherill, J. D. Pritchard, R. P. Abel, M. G. Bason, A. K. Mohapatra, and C. S. Adams, J. Phys. B: At. Mol. Phys. **41**, 201002 (2008).
[17] D. A. Anderson, S. A. Miller, G. Raithel, J. A. Gordon, M. L. Butler, and C. L. Holloway, Phys. Rev. Appl. **5**, 034003 (2016).

[18] M. Saffman, T. G. Walker, and K. Mølmer, Rev. Mod. Phys. **82**, 2313 (2010).
[19] L. Zhang, S. Bao, H. Zhang, G. Raithel, J. Zhao, L. Xiao, and S. Jia, Opt. Express **26**, 29931 (2018).
[20] L. Ma, D. A. Anderson, and G. Raithel, Phys. Rev. A **95**, 061804(R) (2017).
[21] D. J. Whiting, J. Keaveney, C. S. Adams, and I. G. Hughes, Phys. Rev. A **93**, 043854 (2016).
[22] J. Dalibard, Y. Castin, and K. Mølmer, Phys. Rev. Lett. **68**, 580 (1992).
[23] K. Mølmer, Y. Castin, and J. Dalibard, J. Opt. Soc. Am. B **10**, 524 (1993).
[24] H. Saßmannshausen, F. Merkt, and J. Deiglmayr, Phys. Rev. A **87**, 032519 (2013).
[25] E. Arimondo, M. Inguscio, and P. Violino, Rev. Mod. Phys. **49**, 31 (1977).
[26] P. Marte, R. Dum, R. Taïeb, P. D. Lett, and P. Zoller, Phys. Rev. Lett. **71**, 1335 (1993).
[27] G. Raithel, G. Birkl, A. Kastberg, W. D. Phillips, and S. L. Rolston, Phys. Rev. Lett. **78**, 630 (1997).
[28] G. Raithel, W. D. Phillips, and S. L. Rolston, Phys. Rev. Lett. **81**, 3615 (1998).
[29] G. Raithel and N. V. Morrow, in *Advances in Atomic, Molecular and Optical Physics*, edited by M. Scully and G. Rempe (Elsevier, Amsterdam, 2006), Vol. 53, p. 187.
[30] C. P. Pearman, C. S. Adams, S. G. Cox, P. F. Griffin, D. A. Smith, and I. G. Hughes, J. Phys. B: At. Mol. Opt. Phys. **35**, 5141 (2002).
[31] Y. Jiao, J. Li, L. Wang, H. Zhang, L. Zhang, J. Zhao, and S. Jia, Chin. Phys. B **25**, 053201 (2016).
[32] L. Hao, Y. Jiao, Y. Xue, X. Han, S. Bai, J. Zhao, and G. Raithel, New J. Phys. **20**, 073024 (2018).
[33] D. Budker and M. Romalis, Nat. Phys. **3**, 227 (2007).
[34] I. M. Savukov and M. V. Romalis, Phys. Rev. Lett. **94**, 123001 (2005).
[35] B. Patton, O. O. Versolato, D. C. Hovde, E. Corsini, J. M. Higbie, and D. Budker, Appl. Phys. Lett. **101**, 083502 (2012).
[36] P. D. D. Schwindt, S. Knappe, V. Shah, L. Hollberg, J. Kitching, L.-A. Liew, and J. Moreland, Appl. Phys. Lett. **85**, 6409 (2004).
[37] R. Mhaskar, S. Knappe, and J. Kitching, Appl. Phys. Lett. **101**, 241105 (2012).
[38] J. M. Taylor, P. Cappellaro, L. Childress, L. Jiang, D. Budker, P. R. Hemmer, A. Yacoby, R. Walsworth, and M. D. Lukin, Nat. Phys. **4**, 810 (2008).
[39] R. Jiménez-Martínez, W. C. Griffith, S. Knappe, J. Kitching, and M. Prouty, J. Opt. Soc. Am. B **29**, 3398 (2012).